



Full length article

Characterization of local morphology and availability of triple-phase boundaries in solid oxide cell electrodes

G. Rinaldi ^{a, *}, A. Nakajo ^a, P. Burdet ^b, M. Cantoni ^b, W.K.S. Chiu ^c, J. Van herle ^a

^a Group of Energy Materials, École Polytechnique Fédérale de Lausanne, Switzerland

^b Interdisciplinary Centre for Electron Microscopy, École Polytechnique Fédérale de Lausanne, Switzerland

^c Department of Mechanical Engineering, University of Connecticut, Storrs, CT, USA

ARTICLE INFO

Article history:

Received 16 April 2019

Received in revised form

8 July 2019

Accepted 18 July 2019

Available online 27 July 2019

Keywords:

Solid oxide cell cermet

Surfaces available for diffusion

Electro-catalytic sites

3-D electron microscopy

Interfacial curvature

ABSTRACT

The performance of solid oxide cells is known to be dependent upon the density of three phase boundaries (TPB), but the potential for improving their effective electrocatalytic activity by morphological adjustments is imprecisely known. A spilling algorithm was developed to characterize the surfaces available for diffusion at TPBs. It scans each slice in a 3-D imaging dataset to measure the interfaces between the solid and the pore phases at each TPB. Because of the stereological approach, these surfaces are defined as “available lengths” (L_A). The measurement was tested on artificial packed spheres structures with controlled properties and a percolation theory-based model before application to a real Ni-YSZ. The L_A distributions cover 2 orders of magnitude. The subset shorter than the extent of diffusion profiles reported in the literature is in the range of 3% and 20% for Ni and YSZ, respectively, suggesting possible limitations of their effective electrocatalytic properties. The average L_A is larger on YSZ than on Ni, which is a trend opposite to the phase diameter. The available length analysis revealed microstructural characteristics that stem from the manufacturing route and cannot be identified by the inspection of standard metric and topological properties. A strong correlation between the available length and the extension of TPB lines is observed for Ni but not for YSZ, despite the predominance of convex shapes, which likely originates from the Ni reduction. This suggests possibilities for controlling the available length by the manufacturing route, depending specifically on the electrocatalytic properties of the phases in composite materials.

© 2019 Acta Materialia Inc. Published by Elsevier Ltd. This is an open access article under the CC BY-NC-ND license (<http://creativecommons.org/licenses/by-nc-nd/4.0/>).

1. Introduction

The electrochemical performance of solid oxide fuel and electrolysis cell (SOC) electrodes depends on the density and activity of their three-phase boundary (TPB) sites, which are the geometrical intersections between the pore and solid phases in heterogeneous materials. Intuitively, two aspects are relevant for the quality of the sites. First, the transport of oxygen anions, gas species and electrons through the electrode material from the electrolyte, gas channel and electron current collector to the TPB sites must be efficient, e.g. Refs. [1,2]. Second, the morphology near the sites can influence locally the supply of products and reactants that diffuse through the porous composite [3–6].

A variety of composite materials have been developed to obtain

efficient transport, electro-catalytic properties and chemical and mechanical compatibility with adjacent layers and stack components. An example is the Ni-YSZ (yttria-stabilized zirconia) cermet, which is the most widely used fuel electrode material. In a first approximation, the electrode performance scales with the density of connected TPBs. Further analyses show that the local morphology and network topology play a role for the accessibility mainly by the transport of oxygen ions, which can be affected by narrow necks and tortuous pathways [2]. The present study extends the analysis to the characterization of the morphology near the local TPB sites.

The linear relation between the TPB density and the polarization resistance of Ni-YSZ has been established using patterned electrode experiments [7], in which the details of the reaction kinetics were qualitatively analysed [8]. This setup geometry eliminates gas transport limitations that can occur in porous electrodes and facilitates the accurate measurement of the total TPB length. Nevertheless, few studies attempted to analyse specifically the impact of

* Corresponding author.

E-mail address: giorgio.rinaldi@epfl.ch (G. Rinaldi).

surface-diffusion processes associated to each elementary step on the charge-transfer resistance. In the case of controlled TPB geometries, this effect is not noticeable, but as stated by Bessler et al. [9] among others, the morphology close to the TPBs is expected to impact performance, limiting the diffusion of surface species under polarization. For this type of calculations, the TPB is not treated as a geometrical line but as a region with a size that represents the extent of the reaction zone [10].

Few studies attempted to investigate the spatial variation of surface coverage under polarization on patterned Ni-YSZ electrodes as a function of “available length”, which corresponds in a 2-D geometry to the width of ribbons on the Ni and YSZ phases. In a reticulate microstructure, such a length relates to the interfacial surface area (ISA) between the pore and solid phases surrounded by TPB lines. The outcome of the analyses mentioned above suggests an extension ranging from a few nanometers to 100 nm on the Ni surface and from 100 nm up to a few microns on the YSZ surface. One such seminal mechanistic study of the hydrogen oxidation and reduction on patterned Ni-YSZ anodes was performed by Vogler et al. [3]. Hydrogen-spillover was identified as the most likely rate-limiting step. Simulations under polarization showed almost no gradient on the Ni surface, while on the YSZ side, surface diffusion profiles were in the range of 100 nm. The difference is principally due to the fast diffusivity of hydrogen on Ni and, in general, it can be stated that adsorption/desorption kinetics are faster than surface diffusion. Goodwin and co-workers [4] adopted a similar approach to that of Vogler et al., but implemented the splitting of the YSZ surface sites into two groups, surface oxygen and zirconium sites. The results were qualitatively similar, with however a higher extension of the diffusion profiles on the YSZ sites reaching up to 2 μm due to the smaller surface diffusion coefficients. Hanna et al. [11] also developed numerical and analytical models for the oxidation of CO. In this case, the simulations indicate a gradient of CO coverage extending up to 10 nm from the TPB at an applied overpotential of 0.5 V.

At a first appraisal, the references discussed above would suggest a limited effect of surface transport, based on the inspection of indirect and averaged measurements of the available length. The actual impact on the overall electrochemical performance remains however imprecisely known, because the complexity of heterogeneous electrode microstructure may result in local limitations in the case of insufficiently extended surfaces at the TPBs.

The advance of x-ray and electron microscopy methods for the 3-D imaging of SOC electrodes enabled the direct measurement of properties such as connected TPB density and interfacial surface areas (ISA) [12]. At a first appraisal and from a strict geometric standpoint, a first estimate of the average available length ($L_{A,av}$) in reticulate SOC microstructures can be calculated as the ratio between the measured ISA (between pore and each solid i) and total TPB density (Eq. (1)).

$$L_{A,av} [\mu\text{m}] = \frac{ISA_{\text{pore}-i}}{TPB_{\text{tot}}} \quad (1)$$

This calculation is expected to underestimate the actual available diffusion length. In a voxelized representation, it indeed assumes that each ISA unit element is assigned to a single TPB unit length, whereas in reticulate electrode microstructures the surfaces available for diffusion are expected to overlap. Table 1 lists examples of average available lengths computed for Ni-YSZ based on published 3-D focused ion beam – scanning electron microscopy (FIB-SEM) studies of pristine materials. The first Ni-YSZ reconstruction is of $17 \times 10 \times 19 \mu\text{m}^3$ with isometric voxels of 7 nm [13]. Additional data from the study by Joos et al. [14] is added for comparison.

The average available length on Ni ranges from 50 to 60 nm for the two cases considered. The references discussed above do not suggest a limitation for the surface transport of species. In contrast, the average available length on YSZ is larger, between 120 and 170 nm. The preliminary results indicate that the first estimate of the average available length provided by Eq. (1) is comparable to the length of diffusion profiles reported in literature. The average available length computed in Table 1 does not account for the complexity of the reticulate Ni-YSZ microstructures. In reality, a distribution of available lengths is expected. Visual inspection of 3-D reconstructions suggests that the subset of available lengths much smaller than the computed average may not be negligible. Consequently, charge transfer may be locally limited at these sites, affecting the overall electrode performance.

The purpose of this study is the 3-D characterization of the distribution of the available length on the solid phases. An algorithm capable of measuring lengths related to each TPB has been developed. Tests on artificial packed spheres structures with controlled properties were performed first for validation, before application of the method to a Ni-YSZ electrode material selected as an example of a real SOC microstructure. The possibilities to obtain detailed information about the microstructure using the developed available length measurement were explored with a focus on the understanding of the relation between the size and shape of TPB regions and the extension of the locally-measured available lengths. A first analysis of the consequences for the electrode performance was performed based upon the lengths of diffusion profiles reported in the literature.

2. Materials and methods

2.1. Experimental

The Ni-YSZ material used for both the functional and supporting layers in SOLIDpower anode-supported cells [15] has been imaged by 3-D FIB-SEM serial sectioning [12,16,17]. The imaged pristine sample comes from a pristine cell after reduction in a short stack at 800 °C. The cell sample was fractured to expose the interface between the Ni-YSZ anode and the YSZ electrolyte, then impregnated, polished mechanically with sandpaper up to 0.5 μm and gold coated.

The region close to the interface with the electrolyte was then imaged by FIB-SEM serial sectioning with a SEM acceleration voltage of 1.7 kV, current of 1.7 nA and 1 μs dwell time (Zeiss Crossbeam 540). Data from the energy-selective backscatter (ESB) and in-lens secondary electron detectors was recorded. Before the acquisition, fiducial marks consisting of grooves embedded into Pt and C coatings for protection and grayscale contrast were milled to adjust the position of the FIB. This procedure allows maintaining the thickness variation of the slices below the nanometer to guarantee isometric voxels and improve the accuracy of the post-processing slice alignment using a Fiji [18] script.

The reconstructed volume was $17 \times 10 \times 19 \mu\text{m}^3$ with isometric voxel sizes of 7 nm. The ESB and in-lens detector data were combined to facilitate the removal of artefacts due to minor resin impregnation and decomposition. A 3-D bilateral filter was applied before segmentation using Matlab routines with calls to Avizo for image gradient and watershed transform computations. As described in Ref. [2] significant changes in the standard metric and topological properties were not observed after resampling at 10 nm.

2.2. Methodology

The method developed to locally measure the available length

Table 1
Total TPB and interfacial surface area for pristine Ni-YSZ from the literature and computed average available length ($L_{A,av}$). ISA values were adjusted by multiplying for the factor $\pi/6$ to estimate the actual surface area from the digitized volume assuming close to spherical shapes.

	TPB_{tot} [$\mu\text{m}/\mu\text{m}^3$]	$ISA_{pore/Ni}^*$ [$\mu\text{m}^2/\mu\text{m}^3$]	$ISA_{pore/YSZ}$ [$\mu\text{m}^2/\mu\text{m}^3$]	$L_{A,av,Ni}$ [μm]	$L_{A,av,YSZ}$ [μm]
Ni-YSZ	9.04	0.53	1.51	0.06	0.17
Ni-YSZ (Joos et al., 2014)	6.79	0.35	0.84	0.05	0.12

(L_A) on the two solid phases associated to each TPB in segmented 3-D FIB-SEM reconstructions is illustrated in Fig. 1. The algorithm scans the reconstructed segmented volumes (Fig. 1a) slice by slice along the 3 directions (X, Y, Z) (Fig. 1b). In this two-dimensional digitized representation, each TPB of unit length is a point and each diffusion surface on a solid phase is a line, defined as the available length L_A . This stereological approach is valid under the assumption that all portions of the structure and all directions of measurement are equally represented (uniformity and isotropy) [12,19]. Moreover, the developed measurement relies on the simplification that in a 3-D structure the diffusion of surface species driven by the electrochemical reaction occurs perpendicularly to the considered TPB of unit length. The real situation is expected to be more complex in particular in narrow regions, where the diffusion gradients may develop following directions where the density of free sites is higher.

An example of the available lengths detected on a section in the 3-D dataset is displayed in Fig. 1c, in blue and red. TPBs (in green) are recognized when all the three phases are present in four

adjacent voxels (e.g. Fig. 1b). The validity of a TPB is treated following a set of rules and the consistency of paths along the solid-pore interfaces with two-dimensional 4-neighborhood, i.e. shared edges, applied first on the four voxels forming the TPB, then an expanded window of 16 voxels.

- In the case two voxels of the same solid phase (white or dark grey in Fig. 1b) are located diagonally, the TPB is not valid because the pore is not connected directly with the remaining solid phase. On the contrary, in the case of two diagonal pores voxels, two distinct TPBs are documented.
- A valid TPB may be discarded if the surrounding voxels do not form a consistent pathway. A 4 by 4 screening window comprising the 12 neighboring voxels to the TPB element is inspected to ensure that the TPB has 4-neighborhood connection with the exterior of the window through both the solid and pore phase voxels in the dataset throughout the potential start of the path. The pore neighboring voxels located in the four

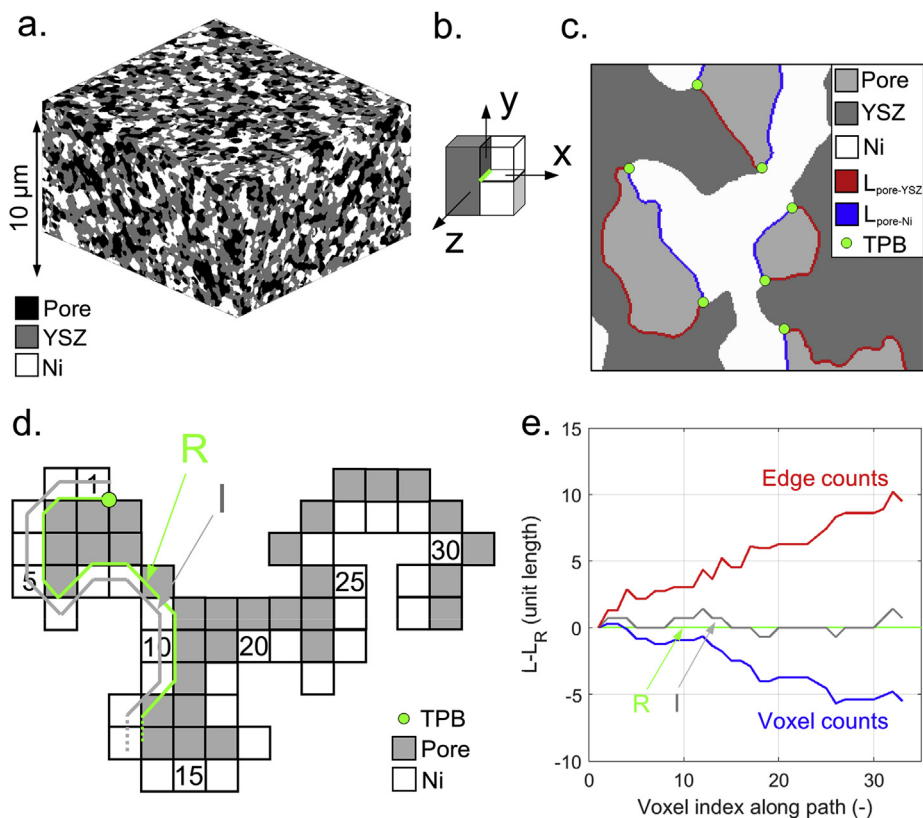


Fig. 1. Overview of the main steps in the measurement of the available length L_A . (a) Ni-YSZ segmented reconstructions considered in this study. View of a TPB of unit length (b., green) detected in the 3-D structure (x-y section). (c.) Example of a cropped section in the 3-D dataset, with TPBs highlighted in green and surfaces for L_A measurements by the spilling algorithm in red and blue. (d.) Illustration of two methods for length measurements using the spilling algorithm, R (green) and I (grey) on a test pattern. (e.) Comparison of the length measured on a test case by the two methods shown in (d.) together with simpler voxel and edge counting; method R is used as the reference L_R . (For interpretation of the references to color in this figure legend, the reader is referred to the Web version of this article.)

corners are discarded if adjacent only to perpendicular solid phases voxels.

- The initial solid voxel connected to the TPB from which the spilling starts must then be identified. In the case of non-unique possibilities, the voxels connected to the pore voxels and with 4-neighborhood connectivity with the solid voxels of the TPB are kept.
- Finally, pore voxels are discarded if not connected to the solid phase at TPB and to its exterior continuation. In the case of diagonal pore voxels intersected by two diagonal solid voxels, only one is considered valid based on its position.

Once the solid voxels outside the TPB are identified, discrete values are assigned for the initial pathway length depending on the possible geometrical combinations within the 4 by 4 window (values equal to 1, 2, 1.707 or 2.707 voxels). This procedure was implemented in an attempt to reduce measurement noise for low lengths, but did not significantly affect the measurements for the structures considered in this study.

The spilling then proceeds over each solid phase along the interface with pores to follow the evolution of the morphology while guarantying the 8-connectivity of the solid and pore phases pathways. The grey line in Fig. 1d (“I”) illustrates how the proposed algorithm proceeds along the pore-solid interface considering 1 voxel in the case of a linear path and $\sqrt{2}$ voxel for a diagonal path. The accuracy provided by methods differing in terms of assumptions and implementation complexity is compared in Fig. 1e. The length measured by the implementation selected for the present study (grey “I” in Fig. 1d) lies in-between simple voxel counts (blue in Fig. 1e) and voxel edge count (red in Fig. 1e), which respectively underestimate and overestimate the length. It provides similar accuracy for the present test case as the method “R” (green in Fig. 1d), which is expected to be more rigorous but more complex to implement. Tests of the proposed algorithm (“I”) on circles further indicate that the error on the measured perimeter is in the range of 8–12% for radii ranging from 100–10 voxels.

The measurement procedure verifies that each voxel belonging to the considered solid phase is in contact with at least one pore voxel to guarantee the consistency of the followed path. The spilling algorithm stops when either another TPB or the exterior of the volume is reached, as visible in Fig. 1c. In the latter case, the measured lengths were documented but not included in the presented results. This also implies that the available length for each TPB is only part of the associated length measured by the spilling algorithm, which can be considered as half in a first approximation (assumption of symmetry in all cases). In addition, the algorithm guarantees consistent behavior when complex bifurcation possibilities are met. In fact, a single length can be shared in rare cases by three different TPBs in the case of singularities or remaining errors from the segmentation process.

In the volumes considered in the present study, approximately 1–2% of the detected TPBs did not comply with the validity and initial 4-neighborhood conditions. 6–9% of the measured lengths were touching the boundary of the volumes and therefore documented but discarded for the analyses. The percentage of lengths that could not be tracked because of bifurcation problems was less than 1%. The list of valid measured lengths is used to generate by binning an estimate of the probability density function for each pore-solid interface, considering either the full list corresponding to the total TPB or the subset of connected TPBs. The common logarithm of the available length is used as an independent variable.

For validation purposes, artificial packed spheres volumes were generated with controlled particle radii, volume fraction and particle neck sizes, as described in Ref. [20]. Besides available length

measurements, standard microstructural properties, i.e., the interfacial surface area, volume fractions, total and connected TPB density were computed using the methods described in Refs. [21,22]. The phase size distributions were calculated based on the phase volume that can be filled with overlapping spheres of a given size e.g. Refs. [23,24] and the coordination number was calculated after skeleton-based partitioning of each phase [2,25].

3. Results and discussion

3.1. Validation

A comparison of the measurements performed in the three primary directions (x,y,z) indicates the isotropy of the considered pristine Ni-YSZ volume in terms of available length (L_A) (not shown). The measured probability densities are spread over about two orders of magnitude and are further characterized by larger noise at lower lengths. As anticipated, the digitized volume representation can be a limitation for the proposed measurement, which does not allow the features of the microstructure close to the spatial resolution of the dataset to be characterized accurately. This is illustrated in Fig. 2a with the probability density distribution of the available length on Ni measured on the volume sample with the native 7 nm isometric voxel size (solid line) and after resampling at 15 nm (dashed line). The difference is small for lengths >20 nm and does not severely affect the global trend in the shape of distribution, but it becomes unstable for smaller lengths. The corresponding thresholds assigned after visual inspection are indicated by the vertical dashed lines. Below this limit, the data is considered statistically unreliable, even though the general trend may still convey qualitative information. Fig. 2a also compares the distributions obtained with the spilling algorithm and the simplest approach in Fig. 1d and e based on the counting of the voxels in the considered solid phase that form the interface with pores (dashed blue line in Fig. 2a). The trend is qualitatively similar, but the spilling algorithm provides increased stability for lengths smaller than 150 nm, which account for more than ~30% of the detected L_A and associated TPBs and henceforth improves the detection capability.

The algorithm was tested on a series of artificially-generated randomly-dispersed packed sphere structures, produced with the in-house code described in Ref. [20]. The computed means of the measured available length distributions (\overline{L}_A) were compared with predictions from a percolation theory-based model. Indeed, the artificially-generated volumes are intuitively expected to comply best with the assumptions of percolation theory, which is based on a representation of the structure as spheres [26]. The details of the percolation model derivation are reported in Appendix A.

The artificial structures were generated by imposing solid volume fractions and fixed particle diameters for the two solid phases (Table 2). A single variation of the intra-phase neck size was also tested (median of the neck size distribution of 0.21 and 0.26 μm). The first five structures have the same combinations of particle sizes but different volume fractions, while the sixth was generated using input values that are close to the measurements on the Ni-YSZ (Section “2.1 Experimental” and corresponding measured properties later in Table 3). The parameters used for the artificial volume generation were used as input to the model based on percolation theory. The computed mean of the available length distribution (\overline{L}_A) and the calculation by the percolation theory model are listed in Table A1.

The comparison between the available length (i) measured on the artificial packed sphere and 3-D electron microscopy volumes and (ii) computed by the percolation model is summarized in Fig. 2b. The ratios of the mean of the available length distributions ($\overline{L}_{A, Ni} / \overline{L}_{A, YSZ}$) measured on the packed spheres and real structures

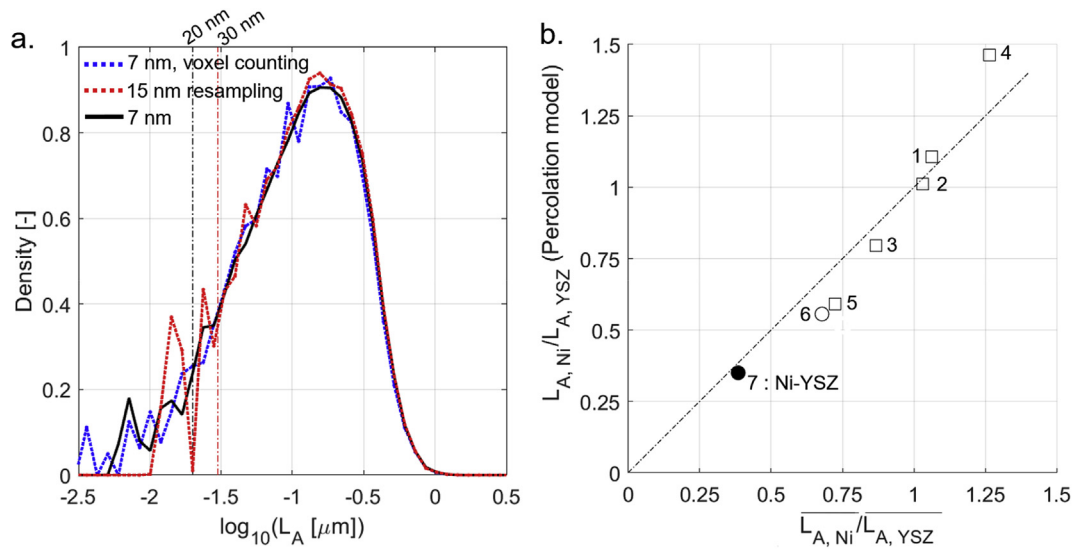


Fig. 2. (a) Computed distribution of available length on Ni in a Ni-YSZ sub-volume with 7 nm voxels and after resampling at 15 nm with the measurement method “R” and voxel counting in Fig. 1. The vertical dashed black line corresponds to a threshold under which the measurement is unstable for the standard 7 nm measurement. (b) Comparison of the available length ratios ($L_{A,Ni}/L_{A,YSZ}$) computed by the percolation theory-based model (y-axis) to that calculated using the spilling algorithm ($L_{A,Ni}/L_{A,YSZ}$ on the x-axis) for the packed spheres (points 1–6) and Ni-YSZ volume imaged by FIB-SEM serial sectioning (point 7). The L_A values are reported in Table A1.

Table 2

Input parameters for the generation of the artificial packed spheres volumes and calculations with the percolation theory model (description in Appendix A).

		Particle diameter [μm]		Volume fraction [-]		
		YSZ	Ni	Pore	YSZ	Ni
1	“small necks”	0.51	0.51	0.37	0.29	0.34
2	“large necks”	0.51	0.51	0.36	0.30	0.34
3	“Intermediate Ni vol. frac.”	0.51	0.51	0.32	0.37	0.31
4	“High Ni vol. frac.”	0.51	0.51	0.32	0.27	0.41
5	“Low Ni vol. frac.”	0.51	0.51	0.32	0.42	0.26
6	“High Ni diameter”	0.47	0.56	0.33	0.43	0.24

are reported on the x-axis. The ratios of the available lengths computed with the percolation model lie on the y-axis. The overall alignment along the 45° dashed line highlights the qualitative agreement between the two approaches for the artificial structures, as well as for the investigated Ni-YSZ material. Analyzing the artificial structures with same diameter (corresponding to points 1 to 5 in Fig. 2b), points 1 and 2 are almost adjacent on the chart despite the differences in neck size among particles. The ratio appears to increase monotonically with that of the volume fraction of the second phase (Ni, points 1–5). Point 6 also follows this trend in the available length measurement dataset, despite the differences in diameter. The black circle 7 referring to the real Ni-YSZ structure is characterized by lower ratios. In this case, the input diameters for the percolation model were selected by choosing the median of the phase size distribution measured by the code described in Section

“2.2 Methodology”, while the ratios on the y-axis were retrieved from the available length distributions discussed later in Fig. 3.

The available lengths computed with the percolation theory-based model depend on the estimated specific surface of the spherical particles (S_{i-j}) and the inter-phase coordination number (Z_{i-j}), as expressed in Eq. A12. This is in line with the observed dependence on the volume fraction, which is reflected on the magnitude of the ratios of measured ISAs (4: $ISA_{Pore-Ni}/ISA_{Pore-YSZ} = 1.46$ and 5: 0.59, see Table A1). In fact, the phases are complex and reticulate in the real Ni-YSZ structure (points 7), resulting in a lower ratio of 0.35, compared to the more homogeneous packed sphere volumes generated with similar volume fraction and mean phase diameter. This implies a lower ratio in Fig. 2b.

3.2. Available length in the Ni-YSZ microstructure

The quantitative agreement between the available lengths measured by the spilling algorithm on artificial structures and model predictions suggests that the developed measurement captures from a volume-averaged perspective the expected dependence on the variation of standard microstructural parameters, such as volume fractions and particle sizes. The results also suggest that the percolation-based model can capture trends for the real Ni-YSZ structure. The model does however not inform about the distribution of the available length, which is a limitation for the precise analysis of the size and shape of TPB regions. The detailed analysis of the Ni-YSZ real structure in this section is therefore performed using the developed spilling algorithm.

As described in Section “2.2 Methodology”, the detected available lengths that touch the boundary with the exterior are

Table 3

Median phase size (d_{50}), volume fraction and mean available length (\bar{L}_A) measured on the Ni-YSZ volume.

	d_{50} [μm]		Volume fraction [-]			Mean L_A [μm]		L_A touching border [%]		L_A from percolation model [μm]	
	YSZ	Ni	Pore	YSZ	Ni	YSZ	Ni	YSZ	Ni	YSZ	Ni
Ni-YSZ	0.37	0.45	0.28	0.43	0.29	0.42	0.16	9.4	6.2	0.07	0.03

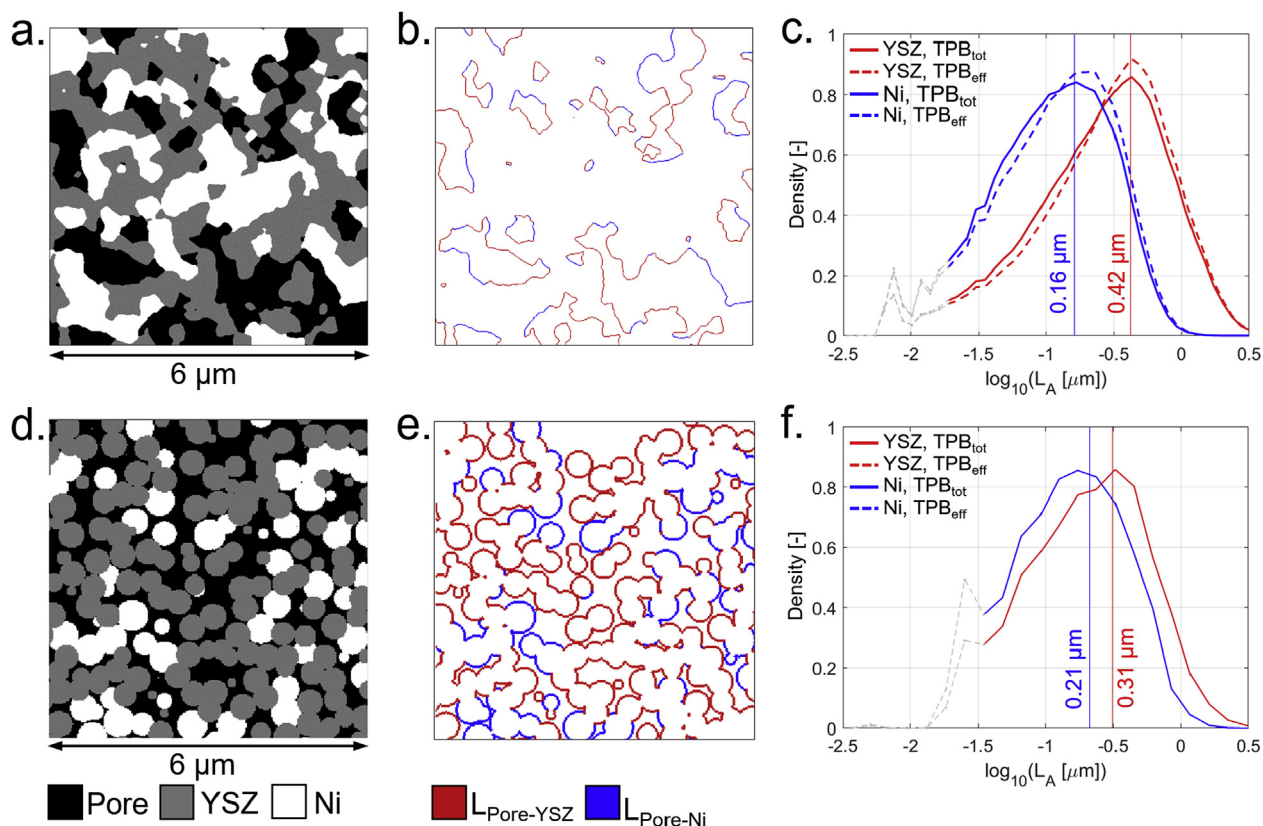


Fig. 3. (a) and (d): cropped 2-D sections respectively from the Ni-YSZ and 6th packed spheres volume. (b) and (e): view of the corresponding detected available length lines (blue for Ni, red for YSZ). (c) and (f): available length distributions obtained with the spilling algorithm measurements. The vertical lines indicate the mean, and the left portion of the distribution shown in grey corresponds to the threshold of 4 times the voxel size. (For interpretation of the references to color in this figure legend, the reader is referred to the Web version of this article.)

discarded for the analysis. However, because of the relatively large size of the two analysed volumes compared to the measured available lengths, still 90–94% are considered valid, which is not expected to affect the relevance of the study (Table 3). The total TPB counts, i.e. half of the spilling iterations, was approximately $4 \cdot 10^6$. The results listed in Table 3 also highlight a limitation of the model based on percolation theory. As discussed previously, the ratio is correctly captured, but not the absolute value. The discrepancy is comparatively less for the packed-sphere volumes (Table A1), which indicates that the Ni-YSZ electrode microstructures significantly differs from a representation by mono-sized phase particles.

The distribution of the available lengths measured in Ni-YSZ are shown in Fig. 3c. The sixth packed spheres volume (number 6 in Table 2) generated using properties similar to the Ni-YSZ FIB-SEM reconstruction is reported for comparison in Fig. 3f. In each plot, the distributions corresponding to the total (connected + unconnected) and effective (connected only) TPBs are displayed with a continuous curve and a dotted curve, respectively. The vertical lines indicate the mean of the distribution \bar{L}_A in the case of total TPBs. The comparison of the ISA and integral of the non-normalized available length distribution informs about the portion of ISA between the pore and the solid phases that is visited by spilling from the TPB, i.e. that is relevant for the electrochemical performance, without however considering overlap among directions.

The distribution of L_A on YSZ is shifted toward larger lengths compared to Ni. This qualitatively depends on the more reticulate YSZ microstructure as illustrated in Fig. 3a and b, where a cropped cross-section in the Ni-YSZ 3-D dataset is displayed with related color-coded available lengths. In particular, the lengths on Ni are on

average shorter and visually less tortuous with respect to YSZ. This trend complies with the ratios of the ISA reported in Table 1, the $ISA_{\text{pore-YSZ}}$ in Ni-YSZ being approximately three times larger than $ISA_{\text{pore-Ni}}$. Hence, the shift between the distribution for Ni and YSZ as well as the computed mean values indicated by the vertical lines follow the expected trend. The mean values of the measured available length distribution L_A is higher than the estimated averaged available length $L_{A,\text{av}}$ presented in Table 1. A reason is that Eq. (1) assumes that each ISA unit element is assigned to a single TPB unit length, whereas the spilling algorithm can visit an ISA unit element several times. Assuming that each available length is shared by two TPBs, the computed mean of the available length distributions corresponds to sufficient values that allow a developed diffusion profile of the surface species up to close to the equilibrium, according to the literature data discussed in the “Introduction”. The difference between the available length distributions for the total and effective TPB density is limited in terms of shape. The slight shift of the distributions toward longer lengths indicates that the available lengths associated to isolated TPBs are on average slightly smaller than the average values.

The available length distributions computed on the artificial structures generated to mimic the Ni-YSZ microstructure (number 6 in Table 3) are provided in Fig. 3f for comparison. Because the structure is made of interconnected spheres, an available length measured by the spilling algorithm can spread over more than one spherical particle, which is not accounted for in the percolation model based on reasoning at the particle scale. There is a correspondence with Fig. 3c, including the mean values. The shape of the distribution for Ni is however better captured than that for YSZ, as

could be anticipated because the latter structure visually deviates more from a packed sphere representation. The measurements also show increased variability for lengths below approximately 4 voxels, for the same reasons as discussed previously in the Section “2.3 Validation”.

3.3. Microstructural analysis

The measured available length distributions indicate that estimates using Eq. (1) or the percolation theory are limited to the discussion of trends related to the trade-off between TPB density and ISAs. In this section, the microstructural information provided by the developed available length measurement is investigated in further detail, in particular with regard to the morphology near the TPBs. A first extension of the analysis provided in the previous section is to analyse the relationship between the two available lengths on each phase associated to a same TPB. Indeed, the electro-catalytic activity of a TPB can be limited by the morphology of one of the two pore-solid interfaces (or both (hereafter referred to as “individual” (I) and “combined” (II) limitation, respectively), as illustrated in Fig. 4a.

The occurrence of the combined and individual limitation cases illustrated in Fig. 4a is investigated by generating the bi-variate probability density of the available length (Fig. 4b). The results indicate a correlation between the available length on Ni and YSZ, e.g. TPBs with a large available length on Ni also benefit from a larger available length on YSZ. The contrary is less clear, which suggests that the local extent of the $ISA_{\text{pore-YSZ}}$ does not necessarily

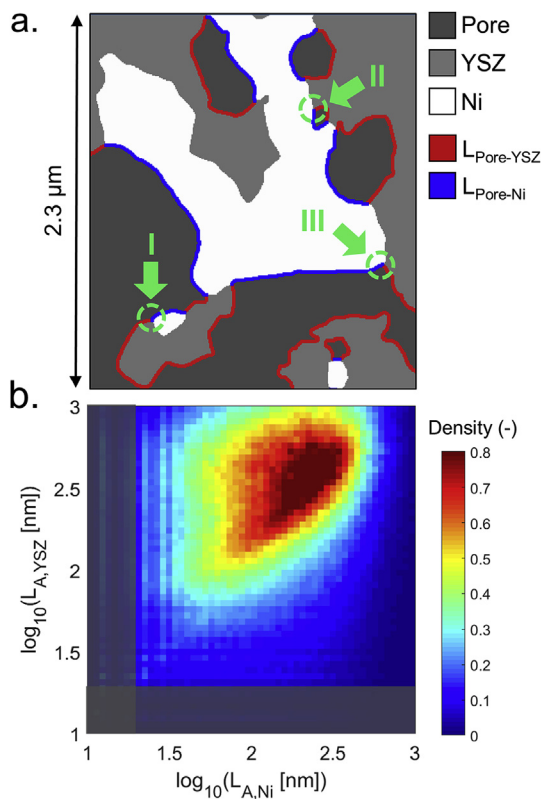


Fig. 4. (a): Example of combinations of Ni and YSZ available lengths (blue and red) at selected TPBs (green circles), showcasing situations where the available lengths on either one (I) or two (II) solid surfaces, or neither (III), may affect performance. (b) Bivariate available lengths distributions associated to same TPB in Ni-YSZ. The regions below the threshold under which the data is considered statistically unreliable is shaded in grey. (For interpretation of the references to color in this figure legend, the reader is referred to the Web version of this article.)

influence that of $ISA_{\text{pore-Ni}}$. The bivariate distribution is almost not populated below the 45° line, indicating that the constraint $L_{A,YSZ} > L_{A,Ni}$ locally holds in the microstructure. These characteristics are not observed in the artificial packed spheres structures (not shown) and they may arise from the manufacturing route of the Ni-YSZ cermet. The synthesis starts with the sintering of the NiO and YSZ powders at around 1400°C , followed by the reduction of NiO around 800°C , which results in an increase in porosity from typically 8% to 27–29% for the studied Ni-YSZ material [13]. The comparatively high sintering temperature (e.g., LSM-YSZ composites are sintered at lower temperature) and foremost significant concurrent movement of the Ni phase therefore results in a pristine Ni-YSZ microstructure that deviates from the random distribution obtained after powder mixing. Indeed, the relocation of the Ni phase on YSZ is expected to favor configurations of low energy.

The manufacturing route of Ni-YSZ materials may further result in a relation between the shape of the TPB lines and the local morphology, which conveys microstructural information. To test this possibility, the available length data is in a first step projected on the 3-D sample volume to visually appreciate the relation between the shape of the TPB lines and the local morphology. For each solid phase, the data retrieved by scanning in the three directions is merged into a single volume for display and object-based analysis. Each TPB element, i.e. the 4 voxels forming a TPB of unit length is assigned a value corresponding to the measured available length (rescaled over 16 bits), keeping the higher value in the case of voxels forming TPBs oriented in different directions. The rationale for this simplification is that the electrochemical reaction is less or not limited at all if the length in one direction is sufficient.

In a second step, the TPB lines are identified as distinct objects in the 3-D dataset to quantitatively investigate the potential correlation between their shape and available lengths. For this purpose, labelling and skeletonization are combined, for the separation into TPB objects and their classification, respectively. The number of disconnected spatial graphs in the Ni-YSZ volume, i.e. of separate TPB skeleton line objects is approximately 12000. For each solid phase, the arithmetic average of the available length on each TPB line is computed. The skeletonized TPB regions are further classified into two categories defined as “loops” and “open lines”. As the names suggest, the first corresponds to a mildly tortuous circular path without starting or ending points. In principle, all the TPB regions should form a closed path or traverse the full electrode volume. In the present case, the “open lines” therefore reach the boundary of the volumes with the exterior. However, a discontinuity in the TPB line is seldom induced because of the low percentage of TPBs identified as not valid by the spilling algorithm, as discussed in Section 2.2 Methodology.

Fig. 5a–d shows the reconstructed TPB lines with color-coded available length. A selected sub-volume instead of the full data is shown for visualization purpose. The inspection of Fig. 5a and b suggests qualitative relationships between the shape of TPB lines and range in L_A in the color scale for Ni in Ni-YSZ. Shorter TPB loops seem to correspond to smaller L_A (Fig. 5b). Further, the Ni available lengths in the longer and less tortuous open lines or loops correspond to larger available lengths. A clear relation is in contrast difficult to assess for YSZ (Fig. 5c and d).

The quantitative analysis of the TPB lines is shown in Fig. 6. The bivariate distributions with the length of the TPB line objects and corresponding average available lengths as independent variables were generated from the 3-D object dataset. The fraction of TPB objects that are open lines is 0.29. Interestingly, a pronounced correlation between the size and available length on Ni is observed, especially for the TPB loops smaller than approximately 100 nm (Fig. 6c). A similar but much less pronounced pattern is observed for the Ni open lines (Fig. 6d). The distribution for YSZ is very

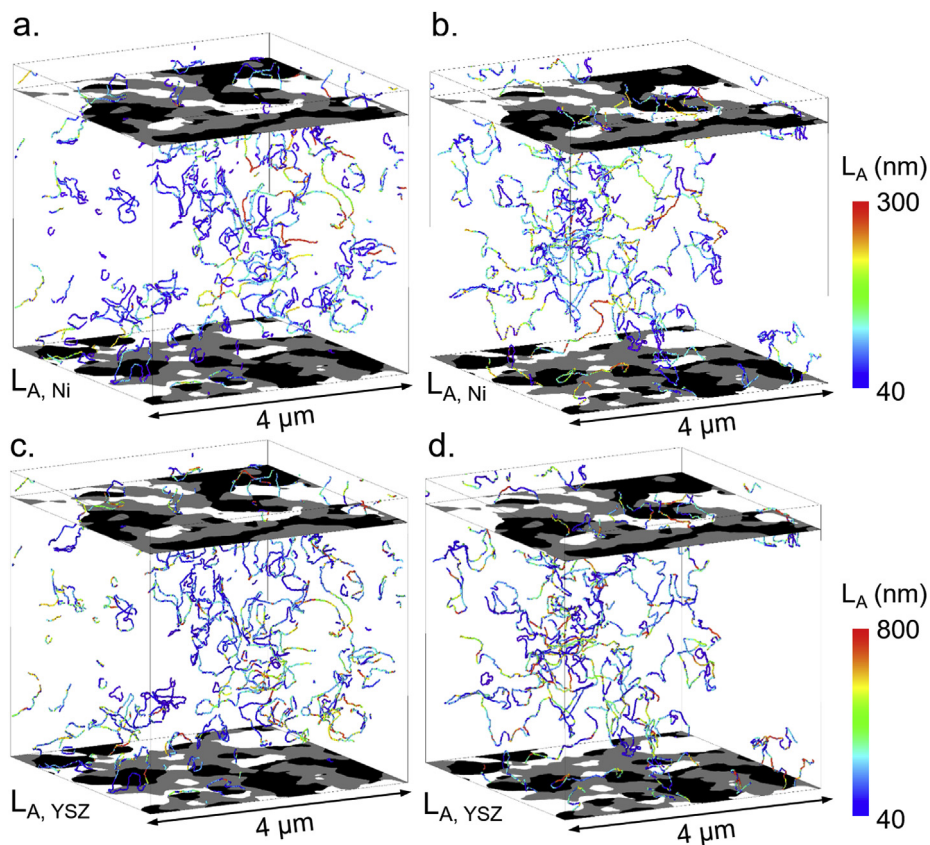


Fig. 5. Regions of interest showing TPB lines with color-coded available length in Ni-YSZ (a–d). Available lengths on Ni in Ni-YSZ corresponding to the subset of closed loops (a, note that part of the loops connect outside from the region of interest) and open lines (b). (c,d) Same representation for the available lengths on YSZ in Ni-YSZ. (For interpretation of the references to color in this figure legend, the reader is referred to the Web version of this article.)

different and a clear correlation is not observed (Fig. 6a and b). It is here worth mentioning that the shortest TPB open lines correspond to fragments near the sample volume boundaries.

The correlation highlighted in Fig. 6c and d further confirms that the Ni phase after reduction has a distinct morphology compared to the ceramic phase. Fig. 7 suggests that the shape of the TPB lines is predominantly controlled by the spatial distribution of Ni, likely because in a first approximation only the Ni phase is mobile and redistributes upon reduction, which is qualitatively supported by the sharper and wedgier microstructure observed in Fig. 3a. Consequently, the relocation of the Ni phase characterized by higher mobility and lower melting temperature must adapt to the morphology of the YSZ.

A Ni particle (in red, translucency) constrained in the YSZ structure (light grey) is shown in Fig. 7a with a TPB line (red, loop). The location complies with the expected Ni dihedral angle ($\sim 150^\circ$) [27]. The available length on Ni in this specific configuration is dependent upon the radius of the particle in each slice considered, and therefore on the Ni morphology. This is illustrated qualitatively in Fig. 7b where a larger Ni particle is shown. YSZ lengths on the other hand do not exhibit a clear dependence in both cases. The Ni particle displayed in Fig. 7a is isolated and does not percolate with the other Ni regions, thus the TPB is not connected. Indeed, shorter closed TPB rings have a higher probability to be related to the junction of an isolated small inclusion and a much larger region of the opposite phase. This qualitative analysis however seems to hold for larger inclusions such as shown in Fig. 7b and c, for convex and concave Ni shapes.

The analysis of the correlation observed in Fig. 6 based upon

selected cases shown in Fig. 7 is qualitative. Curvature analysis has been performed to include the variety of shapes in the Ni-YSZ heterogeneous microstructure. The description of the curvature measurement procedure is provided in Appendix B). Fig. 8a–c report the ISDs (interfacial shape distributions) of the three ISA interfacial area combinations. The fraction of the surface corresponding to each of the four main shape categories is indicated in white. The diagonal dashed line with negative slope corresponds to constant mean curvature $(\kappa_1 + \kappa_2)/2$. In particular, the line that separates the two saddle regions is characterized by null mean curvature.

The distribution of YSZ shapes is similar for the pore/YSZ (Fig. 8a) and Ni/YSZ (Fig. 8c) subsets, with ISDs mostly populated in the second and third regions corresponding to saddle shapes. This is in line with the hypothesis that the ceramic phase mainly acts as a matrix limiting the Ni relocation. The Ni surface facing pore (mirror of Fig. 9b) appears comparatively shifted toward saddles of the second type and dimples. This is visually confirmed by Fig. 3b, which indicates that the interface between Ni and pore is slightly concave. This specific arrangement of Ni after reduction differs from a packed sphere representation. It is intuitively controlled by the large Ni dihedral angle ($\sim 150^\circ$) [27] and minimization of surface area with highest energy γ ($\gamma_{\text{Pore/Ni}} > \gamma_{\text{Ni/YSZ}} > \gamma_{\text{Pore/YSZ}}$) within the constraint imposed by the YSZ scaffold. In this regard, the results indicate that the Ni surface enclosed between two YSZ regions has a slightly concave, rather than convex shape, where the kinetics of Ni reduction may play a role. The relationship between formed TPB lines and L_A illustrated in Fig. 7 can also apply in a simplified view to Ni hourglass shapes constrained by YSZ. Indeed, narrow necks in

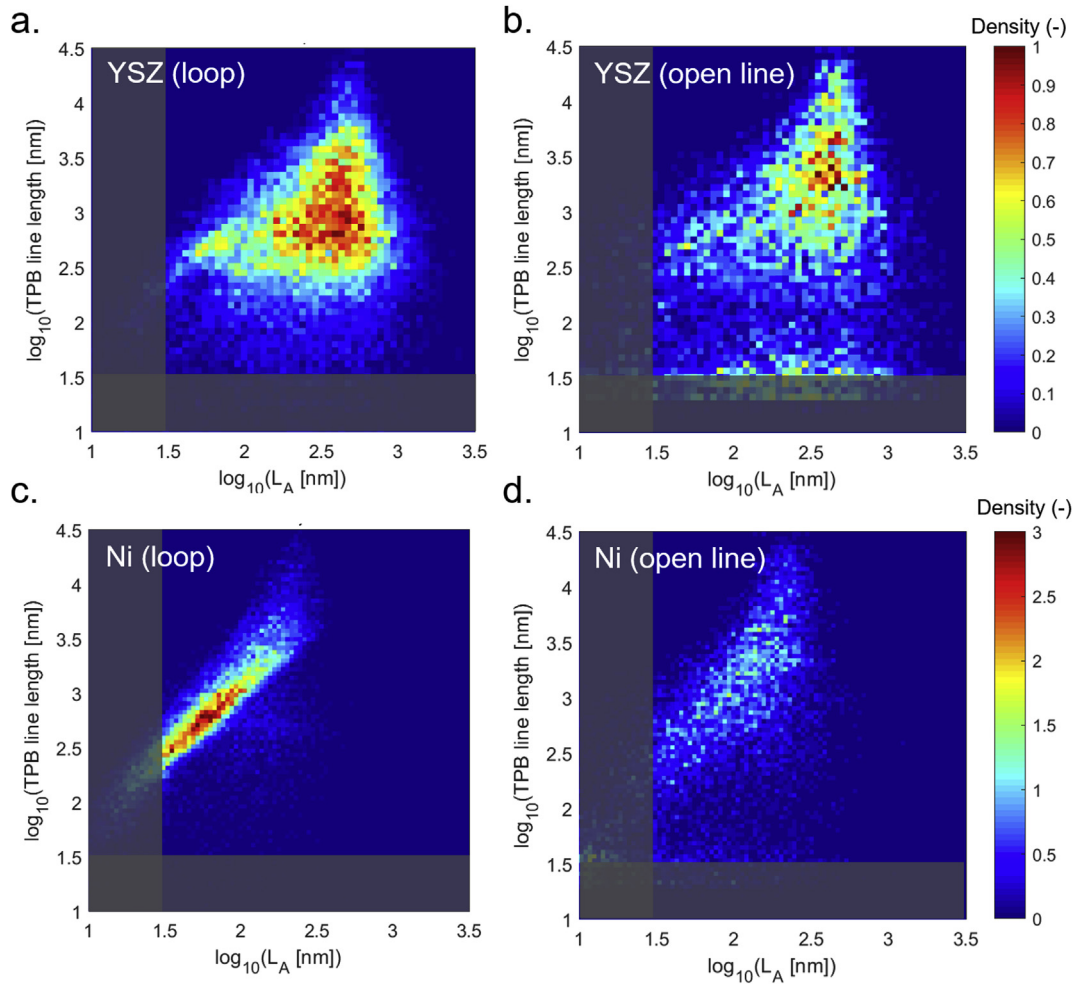


Fig. 6. Bivariate distribution of available length L_A and corresponding TPB object lengths for YSZ (a,b) and Ni (c,d) in Ni-YSZ. (a) and (c) correspond to the subset of TPB line objects forming loops, whereas (b) and (d) refer to that of open-lines.

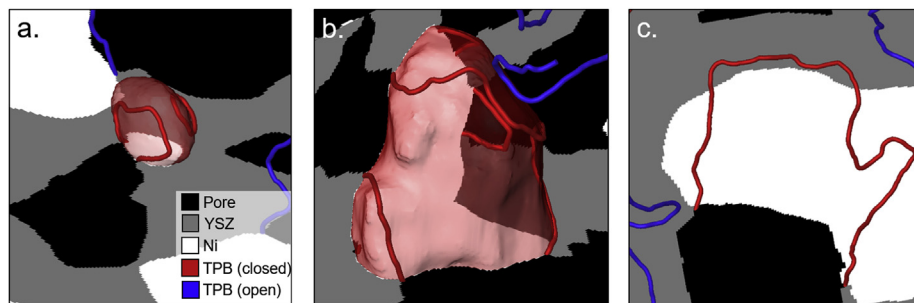


Fig. 7. Selected close-up views in the Ni-YSZ dataset showing TPB loops (red) and open lines (blue) near isolated Ni particles (a, b: red, translucency) and connected regions (c). (For interpretation of the references to color in this figure legend, the reader is referred to the Web version of this article.)

slender shapes are likely to pinch-off and therefore populate the “bump” region in the ISD. The fraction with cylindrical shapes is also significant for the Ni/YSZ interfaces, which is in line with the need for the Ni phase to be located on YSZ regions where the dihedral angle condition is fulfilled.

3.4. Implications for electrode performance and microstructural design

The available length analysis clearly revealed features of the Ni-

YSZ microstructure that stem from the manufacturing route and cannot be identified by the inspection of standard metric and topological properties. The results in Section 3.2 and Eq. (1) indicate first that design in the view of the maximization of the TPB density may not be optimal for all composite electrodes. Second, the presence of correlations between TPB line objects and $L_{A,Ni}$, as well as the constraint $L_{A,YSZ} > L_{A,Ni}$ (Section 3.3), lets anticipate potential for improving the effective electrocatalytic activity of state-of-the-art electrode materials by guiding the selection of manufacturing methods and parameters depending upon the properties of the

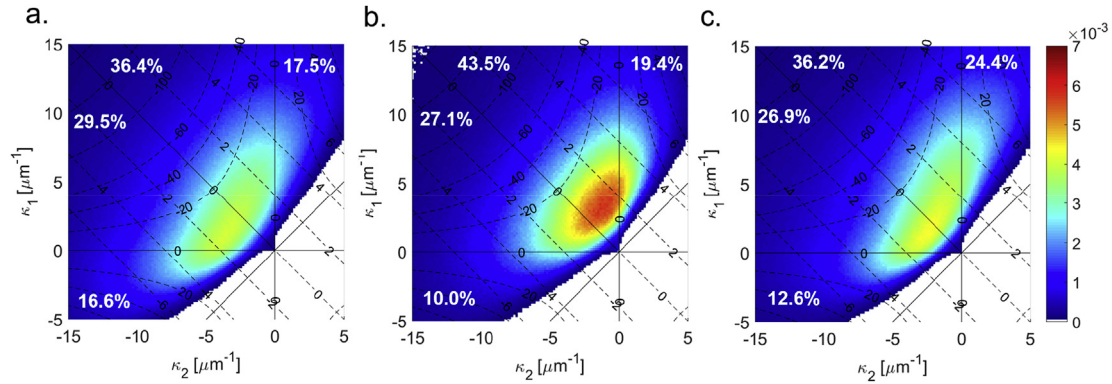


Fig. 8. ISD plots related to the three interfacial surfaces in Ni-YSZ, respectively pore/YSZ (a), pore/Ni (b) and Ni/YSZ (c) interfaces. The percentages indicate the fraction of the surface area corresponding to the four zones.

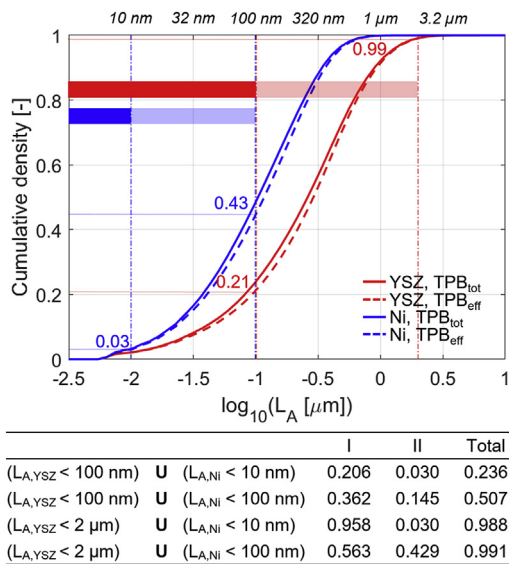


Fig. 9. Cumulative distribution of the available lengths measured on Ni-YSZ. The vertical dashed lines and horizontal coloured bars (in transparency) indicate the range of diffusion profile length reported in the literature (Ni: Vogler et al. [3], Goodwin et al. [4], Hanna et al. [11], YSZ: Vogler et al. [3], Goodwin et al. [4]). The lower table provides the fraction corresponding to the limitation classification (I and II) illustrated in Fig. 4a.

bulk phase material. Indeed, differences in the elementary steps in the reactions and surface transport properties result in specific requirements in terms of the three situations illustrated in Fig. 4a for an optimal balance between TPB density and available length.

The distributions in Fig. 3c, f indicate that the subset of available lengths smaller than the diffusion profiles discussed in the Introduction can be larger than a few percent, which is quantified in Fig. 9a. The latter provides the cumulative distribution of available lengths together with the estimated extensions of the diffusion profiles under polarization reported in the literature for Ni-YSZ (vertical dashed lines and shaded area). For such lengths, a limitation on the spillover reaction may occur, consequently on performance at these electrocatalytic sites, even if the TPB is connected and highly accessible. The percentage of measured available lengths lower than indicative thresholds are respectively 3–43% and 21–99% for Ni and YSZ. The vertical dashed lines indicate the lower value together with the range of variation in transparency (horizontal bars), showcasing that a strong uncertainty on the exact percentage remains. The ranges reported in the literature suggest that the morphology of the Ni phase is less critical for the

performance than that of the YSZ phase. In particular, according to Goodwin [4], the surface diffusion profile on YSZ may exceed 2 μm , which would be problematic for most of the TPB sites detected in the present Ni-YSZ material.

In the Ni-YSZ case treated here, the higher YSZ volume fraction for sufficient ion conduction and the observed inequality $L_{A,YSZ} > L_{A,Ni}$ appears beneficial. Fig. 9 however indicates that the microstructure is not ideal in terms of the trade-off between available length and TPB density. Indeed, the optimal use of ISAs would be characterized by narrow L_A distributions with the peak at values at or slightly larger than the corresponding diffusion profile. The table in Fig. 9 provides the fraction of connected TPB potentially subjected to limitation for the 4 possible combinations from the diffusion profile lengths reported in the literature and the breakdown for single or combined limitation. The results slightly differ from an analysis of each phase separately. They also indicate that the subset $L_{A,Ni} < 10 \text{ nm}$ relates to small features on YSZ as well and is subjected to combined limitation (II) in any case, despite the conditions $L_{A,YSZ} > L_{A,Ni}$.

An available length slightly shorter than required for fully developed diffusion profiles on one or both surfaces may not be necessarily critical for the performance, but the determination of threshold values for acceptable performance penalty will require dedicated mechanistic charge-transfer studies and experimental validations. Besides changes in phase materials, differences in requirements on the available length can be also anticipated for a same composite, i.e. compared to the literature data used in Fig. 9 for Ni-YSZ, depending upon the electrode operation conditions. Typical examples that warrant future analyses are methane steam reforming and co-electrolysis, which are catalysed by Ni.

It is worth mentioning that Ni-YSZ is affected by microstructural degradation during operation [27–30] that is expected to modify the available length. The decrease in TPB density proceeds initially rapidly because of the fast rearrangement of the pore and Ni phases and then coarsening is slower typically after a few hundred hours [31–33]. The available length on Ni is intuitively expected to increase. Therefore, an additional significant degradation contribution due to that of the electro-catalytic properties of the TPB sites is not expected. A coarser Ni phase may result in changes in the available length on YSZ as well, but a detailed analysis will be required. The sensitivity of the available length measurement to differences in the microstructure that could not be anticipated by standard metrics may here also help to better describe the degradation of the Ni-YSZ microstructure in future.

The microstructural analysis in Section 3.3 indicates that differences in mobility during manufacturing (e.g. contrast in sintering properties and/or induced by chemical changes) between the

phases, as well as wettability are relevant for controlling the available lengths, depending on the corresponding materials' electrocatalytic properties.

From the standpoint of sintering of randomly-dispersed powders and fixed combinations phase materials, the higher the difference in sizes between the particles of a same phase, the broader the associated distribution of available length, leading to an imperfect use of the interfacial surface area. The portion of shorter available length (left portion of the distribution) may cause limitation, while prolonged lengths do not provide benefit. Therefore, a small spread in the initial powders' sizes can facilitate the fabrication of microstructures with more predictable properties, independently of the sintering conditions. The L_A measurements on artificially-generated packed sphere structures however demonstrate that this consideration remains largely imprecise, because of phase network topology (Fig. 3d–f). In the case of very short diffusion profiles, the usual target of maximized TPB density is adequate, within the constraints of connectivity and accessibility considerations. If the extension of the diffusion profile is larger yet similar for both the solid phases (ratio in Fig. 2b approximately equal to one), the average available length scales with the phase size, even if in the case of a coarse phase, sufficiently low wettability must be guaranteed to maintain adequate ISA with pores. An increased volume fraction yields at a first appraisal a greater number of particles, more extended surface area and therefore average available length. Similar reasoning can be applied if the imbalance between the two phase is very large, i.e. the surface of one phase is not relevant for the charge-transfer rate, until the penalty on charge transport becomes dominant.

4. Conclusions

The electrochemical performance of solid oxide cell electrode composite materials is known to be dependent upon the density of TPBs and their accessibility by the transport of gas species, electrons and ions. This study investigates the additional potential effect of the local morphology near the TPBs. It is focused on the characterization of the extension of the surface on the two solid phases at each TPB, because a narrow or restricted surface may limit the diffusion of the surface species involved in charge-transfer and therefore affect the electrochemical performance.

A spilling algorithm was created to measure the available length, a property to quantify the extension of regions available for surface diffusion on 3-D reconstructions obtained by e.g. x-ray nanotomography or focused-ion beam – scanning electron microscopy. The current approach is stereological and consists in scanning the 3-D volumes slice by slice in 3 directions, where TPBs are points and each diffusion surface a line. The available length was first measured in a set of artificially-generated packed sphere structures with controlled properties for validation. The results were successfully compared with a percolation theory-based model, which expresses the dependence of the available lengths on the interfacial surface areas and coordination number of the solid phases expected for such structures.

A real Ni-YSZ electrode was selected as a first study case and imaged by FIB-SEM. The measured distributions of available lengths indicate a spread over about 2 orders of magnitude. The available length was larger on YSZ than Ni, which is a trend opposite to the phase diameter. The subset of TPBs with electrochemical performance potentially affected by the local morphology may not be negligible, 3–43% and 21–99% for Ni and YSZ, based on the estimated lengths of the diffusion profiles from the literature. This result warrants targeted efforts to quantify the effect, which is classically overlooked in analyses based upon TPB density and effective phase transport properties.

The relation between the two available lengths at each TPB, as well as the size of the TPB regions were investigated with the support of interfacial shape distributions computed by curvature analysis. The results highlighted microstructural characteristics, which cannot be identified by the inspection of standard metric and topological properties. The relatively high sintering temperature for NiO-YSZ and the reduction of Ni involved in the synthesis yields a microstructure where a clear relationship exists between the phase size, available length, extension and shape of the TPB regions, mostly for Ni. In particular, TPBs with a large available length on Ni also benefit from a larger available length on YSZ. Further, small available lengths often correspond to isolated TPBs, as expected from the relationship with the local Ni phase size.

The study indicates first that design in the view of the maximization of the TPB density may not be optimal for all composite electrodes. Differences in the elementary steps in the reactions and surface transport properties should be accounted specifically for each phase. Second, the inspection of Ni-YSZ microstructure suggests possibilities for tailoring the available length by adjustments of the manufacturing route, sintering properties and material dihedral angles. The sensitivity of the available length measurement to differences in the microstructure, which could not be anticipated by standard metrics, may also help to better describe the degradation of the Ni-YSZ microstructure and the impact on performance after aging.

Acknowledgements

This work was supported by the Swiss EOS Holding Ph. D. thesis funding (G. Rinaldi), contract 2014-0365. The research also received funding from the Fuel Cells and Hydrogen 2 Joint Undertaking under grant agreements No 735692 (Project name: CH2P), No 735918 (Project name: INSIGHT), No 731224 (Project name: BALANCE) and No 699892 (Project name: ECo). This Joint Undertaking receives support from the European Union's Horizon 2020 research and innovation program, from Hydrogen Europe and Hydrogen Europe Research. Swiss partners in these H2020 projects receive funding from the Swiss Secretariat in Education, Research and Innovation (SEFRI), under contracts 16.0199 (Insight), 16.0223 (CH2P), 16.0178 (Balance) and 16.0041 (ECo). WKSC acknowledges financial support from the National Science Foundation (Award CBET-1134052), and an Energy Frontier Research Center on Science Based Nano-Structure Design and Synthesis of Heterogeneous Functional Materials for Energy Systems (HeteroFoAM Center) funded by the US Department of Energy, Office of Science, Office of Basic Energy Sciences (Award DE-SC0001061). The authors would like to thank Dr. A. P. Cocco (Army Research Laboratory, Adelphi, MD) for the collaboration on the curvature measurements, M.B. DeGostin and P. J. Damian (UConn) for the generation of packed-sphere volumes, and Dr. D. Montinaro and J.P. Ouweltjes (SOLIDpower) for providing the Ni-YSZ material.

Appendix A. Percolation theory-based model for available length calculations

The approach used in this study to estimate the mean available length (Fig. 2b) is based upon percolation theory and the measurement of interfacial surface areas (ISA) in 3-D volumes. The data for the artificial structures and electrode microstructures imaged by FIB-SEM in this study are reported in Table A1). Percolation theory relies on the prediction of coordination numbers, i.e., number of contacts among neighboring spherical particles. Hence, the number fraction of the solid phase i in the binary mixture containing solid phases i and j is defined in Eq. (A1). For the sake of brevity, equations only for the phase i are provided in the following

description.

$$N_i = \frac{\frac{\Psi_i}{r_i^3}}{\frac{\Psi_i}{r_i^3} + \frac{\Psi_j}{r_j^3}} \quad (\text{A1})$$

where Ψ_i and r_i are the solid volume fraction and the radius of the phase i , respectively.

The total coordination number for the solid phase i (Z_i) is computed according to Eq. (A2) [26]. The value of the overall average coordination number of all solid particles \bar{Z} is often set equal to 6, based on estimation from synthetic packed spheres structures [34,35]. It was set equal to 5.3 for the Ni-YSZ and LSM-YSZ, which corresponds to measurements performed for electrode materials such as investigated in this study in Ref. [2] using a discrete representation of the microstructure provided by skeleton edge and vertices-based partitioning.

$$Z_i = 3 + \frac{\bar{Z} \times r_i^2}{N_i \times r_i^2 + N_j \times r_j^2} \quad (\text{A2})$$

The intra and inter-phase coordination numbers are expressed in Eqs. A3 and A4, respectively.

$$Z_{i/i} = \frac{\bar{Z} \times \frac{\Psi_i}{r_i}}{\frac{\Psi_i}{r_i} + \frac{\Psi_j}{r_j}} \quad (\text{A3})$$

$$Z_{i/j} = \frac{N_i \times Z_i \times Z_j}{\bar{Z}} \quad (\text{A4})$$

The number of particles per unit volume n_i^V is computed as the ratio between the volume fraction φ_i and the spherical volume of the solid phases i (Eq. (A5)). Even if the estimated value for hard spheres is expected inferior than the actual number of particles present in artificial packed spheres volumes, because of the overlap to manipulate the neck size, it can be considered valid as long as the contact angles among particles do not exceed 30° [36].

Table A1

Properties measured on the artificial packed spheres volumes.

	Volume size [voxel ³]	Voxel size [nm]	ISA [$\mu\text{m}^2/\mu\text{m}^3$]			Mean L_A [μm]		L_A percolation [μm]		
			Ni/LSM-Pore	YSZ-Pore	Ni/LSM-YSZ	Ni/LSM	YSZ	Ni/LSM	YSZ	
1	"small necks"	420 × 420 × 420	14	2.32	2.10	0.38	0.32	0.30	0.31	0.28
2	"large necks"	420 × 420 × 420	14	1.93	1.91	0.66	0.26	0.25	0.19	0.19
3	"Medium Ni/LSM vol. frac."	420 × 420 × 420	14	1.93	2.43	0.53	0.25	0.29	0.21	0.26
4	"High Ni/LSM vol. frac."	420 × 420 × 420	14	2.59	1.77	0.53	0.30	0.24	0.28	0.19
5	"Low Ni/LSM vol. frac."	420 × 420 × 420	14	1.62	2.74	0.53	0.23	0.31	0.18	0.31
6	"High Ni/LSM diameter"	270 × 270 × 270	23	1.33	2.38	0.71	0.21	0.31	0.13	0.24

$$n_i^V = \frac{\varphi_i}{\frac{4}{3} \pi r_i^3} \quad (\text{A5})$$

A stereological simplification passing from a 3-D to a 2-D representation shown in Fig. A1 is adopted to compare the direct measurement of the available length by the spilling algorithm with the estimate from the percolation model for mono-sized particles.

The interfacial surface areas ISA_{TOT} per unit of volume in the artificial structures presented in Table A1 were measured using the standard methods described in the section "Methodology". Division by n_i^V provides the amount of surface shared by the i particle with

pores and with the particles of opposite phase (Eq. (A6)).

$$S_{Pore/i} = \frac{ISA_{TOT\ Pore/i}}{n_i^V} S_{i-j} = \frac{ISA_{TOT\ i/j}}{n_i^V} \quad (\text{A6})$$

The shared surface among each couple of particles can be approximated by dividing the coordination number (Eq. (A7)). As mentioned previously, this assumption formally holds in the case of small contact angles.

$$A_{i/j} = \frac{S_{i/j}}{Z_{i/j}} \equiv A_{j/i} = \frac{S_{j/i}}{Z_{j/i}} \quad (\text{A7})$$

As shown in Fig. A1 with dashed red lines, the TPB circumferences at inter-phase contacts are computed with Eq. (A8), and the related radius with Eq. (A9).

$$TPB_{i/j} \equiv TPB_{j/i} = 2\pi \sqrt{\frac{A_{i/j}}{\pi}} \quad (\text{A8})$$

$$r_{TPB\ i/j} \equiv r_{TPBj/i} = \sqrt{\frac{A_{j/i}}{\pi}} \quad (\text{A9})$$

The available length L_{A_i} is computed by gradually expanding a hypothetical annulus (with external radius r_{MAX_i}) until the contact surface $S_{Pore/i}$ is fully covered (Eq. (A10)). Therefore, the ratio between the area of the annulus (with external radius r_{MAX_i} and internal radius $r_{TPB\ i/j}$) and the perimeter of the TPB yields the expression for the available length Eq. (A11).

$$S_{Pore/i} - \pi (r_{MAX_i}^2 - r_{TPB\ i/j}^2) Z_{i/j} = 0 \quad (\text{A10})$$

$$L_{A_i} = \frac{\pi (r_{MAX_i}^2 - r_{TPB\ i/j}^2)}{2 \pi r_{TPB\ i/j}} = \frac{(r_{MAX_i}^2 - r_{TPB\ i/j}^2)}{2 r_{TPB\ i/j}} \quad (\text{A11})$$

Appendix B. Curvature analysis

Curvature analysis was performed to investigate the relation between available length and local morphology. A triangular surface mesh of the three-phase volumes is generated using Avizo's implementation of the marching cube algorithm followed by modified shrinkage-free Gaussian smoothing (two iterations with a vertex displacement weight of 0.6). The surface mesh for each individual phase is then reconstructed using Matlab post-processing routines. The principal curvatures κ_1 and κ_2 at each patch of the reconstructed meshes are measured by Avizo based on a local

quadratic surface fit and four repetitions of averaging among patches sharing common mesh edges (two layers of neighbor patches were considered). The subset of principal curvatures corresponding to each inter-phase surface in the full mesh dataset is finally retrieved using Matlab routines and weighted by the corresponding subset of triangle areas to generate interfacial shape distributions (ISD) [37]. The bi-variate ISD plots can be divided into four distinct regions, respectively bumps (κ_1 and $\kappa_2 > 0$), saddles of the first type ($\kappa_1 > -\kappa_2$), saddles of the second type ($\kappa_1 < -\kappa_2$) and dimples (κ_1 and $\kappa_2 < 0$). Surfaces that lay on the 45° diagonal with positive slope have a spherical shape, while those on the two axes have cylindrical shape. In the case of negative κ_2 , those surfaces surround the void at the interior. The origin of the plot represents a planar surface. The zones $\kappa_1 < \kappa_2$ are not populated, because of the principal curvature definition. It is worth mentioning that interfaces measured from opposite sides (i.e. Ni/YSZ vs YSZ/Ni) would correspond to similar plots reversed over the diagonal line $\kappa_1 = -\kappa_2$ (where the mean curvature is null), e.g. a predominance of dimples is mirrored by a prevalence of bumps in the complementary ISA set.

Appendix C. Supplementary data

Supplementary data to this article can be found online at <https://doi.org/10.1016/j.actamat.2019.07.027>.

References

- [1] P.S. Jørgensen, S.L. Ebbenhøj, A. Hauch, Triple phase boundary specific pathway analysis for quantitative characterization of solid oxide cell electrode microstructure, *J. Power Sources* 279 (Apr. 2015) 686–693.
- [2] A. Nakajo, A.P. Cocco, M.B. DeGostin, A.A. Peracchio, B.N. Cassenti, M. Cantoni, J. Van herle, W.K.S. Chiu, Accessible triple-phase boundary length: a performance metric to account for transport pathways in heterogeneous electrochemical materials, *J. Power Sources* 325 (Sep. 2016) 786–800.
- [3] M. Vogler, A. Bieberle-Hütter, L. Gauckler, J. Warnatz, W.G. Bessler, Modelling study of surface reactions, diffusion, and spillover at a Ni/YSZ patterned anode, *J. Electrochem. Soc.* 156 (5) (2009) B663.
- [4] D.G. Goodwin, H. Zhu, A.M. Colclasure, R.J. Kee, “Modeling electrochemical oxidation of hydrogen on Ni–YSZ pattern anodes, *J. Electrochem. Soc.* 156 (9) (Jan. 2009) B1004–B1021.
- [5] T. Horita, T. Tsunoda, K. Yamaji, N. Sakai, T. Kato, H. Yokokawa, Microstructures and oxygen diffusion at the LaMnO₃ film/yttria-stabilized zirconia interface, *Solid State Ion.* 152–153 (Dec. 2002) 439–446.
- [6] Y. Fu, S. Poizeau, A. Bertei, C. Qi, A. Mohanram, J.D. Pietras, M.Z. Bazant, Heterogeneous electrocatalysis in porous cathodes of solid oxide fuel cells, *Electrochim. Acta* 159 (Mar. 2015) 71–80.
- [7] J. Mizusaki, H. Tagawa, T. Saito, K. Kamitani, T. Yamamura, K. Hirano, S. Ehara, T. Takagi, T. Hikita, M. Ippommatsu, S. Nakagawa, K. Hashimoto, Preparation of nickel pattern electrodes on YSZ and their electrochemical properties in H₂-H₂O atmospheres, *J. Electrochem. Soc.* 141 (8) (Jan. 1994) 2129–2134.
- [8] A. Bieberle, L.P. Meier, L.J. Gauckler, The electrochemistry of Ni pattern anodes used as solid oxide fuel cell model electrodes, *J. Electrochem. Soc.* 148 (6) (Jan. 2001) A646–A656.
- [9] W.G. Bessler, M. Vogler, H. Störmer, D. Gerthsen, A. Utz, A. Weber, E. Ivers-Tiffée, Model anodes and anode models for understanding the mechanism of hydrogen oxidation in solid oxide fuel cells, *Phys. Chem. Chem. Phys.* 12 (42) (Oct. 2010) 13888–13903.
- [10] Y. Zhang, Y. Chen, Y. Lin, M. Yan, W.M. Harris, W.K.S. Chiu, M. Ni, F. Chen, Electrochemical fields within 3D reconstructed microstructures of mixed ionic and electronic conducting devices, *J. Power Sources* 331 (Nov. 2016) 167–179.
- [11] J. Hanna, W.Y. Lee, A.F. Ghoniem, Kinetics of carbon monoxide electro-oxidation in solid-oxide fuel cells from Ni-YSZ patterned-anode measurements, *J. Electrochem. Soc.* 160 (6) (Jan. 2013) F698–F708.
- [12] A.P. Cocco, G.J. Nelson, W.M. Harris, A. Nakajo, T.D. Myles, A.M. Kiss, J.J. Lombardo, W.K.S. Chiu, Three-dimensional microstructural imaging methods for energy materials, *Phys. Chem. Chem. Phys.* 15 (39) (Sep. 2013) 16377–16407.
- [13] A. Nakajo, A.P. Cocco, M.B. DeGostin, P. Burdet, A.A. Peracchio, B.N. Cassenti, M. Cantoni, J. Van herle, W.K.S. Chiu, Evolution of 3-D transport pathways and triple-phase boundaries in the Ni-YSZ hydrogen electrode upon fuel cell or electrolysis cell operation, *ECS Trans.* 78 (1) (May 2017) 3205–3215.
- [14] J. Joos, M. Ender, I. Rotscholl, N.H. Menzler, E. Ivers-Tiffée, Quantification of double-layer Ni/YSZ fuel cell anodes from focused ion beam tomography data, *J. Power Sources* 246 (Jan. 2014) 819–830.
- [15] SOLID power, Home - SOLIDpower [Online]. Available: <https://www.solidpower.com/en/>. (Accessed 19 July 2018).
- [16] K. Yakal-Kremiski, J.S. Cronin, Y.-C.K. Chen-Wiegart, J. Wang, S.A. Barnett, Studies of solid oxide fuel cell electrode evolution using 3D tomography, *Fuel Cells* 13 (4) (2013) 449–454.
- [17] M. Cantoni, A. Nakajo, G. Rinaldi, S. Diethelm, J. Van herle, “Characterization of solid oxide electrolysis cells by advanced FIB-sem tomography,” white pap, ZEISS Atlas 5 (7) (Jun. 2017).
- [18] C.T. Rueden, J. Schindelin, M.C. Hiner, B.E. DeZonia, A.E. Walter, E.T. Arena, K.W. Eliceiri, ImageJ2: ImageJ for the next generation of scientific image data, *BMC Bioinf.* 18 (Nov) (2017).
- [19] J.C. Russ, *Practical Stereology*, Springer US, 1986.
- [20] M.B. DeGostin, A. Nakajo, B.N. Cassenti, A.A. Peracchio, G.J. Nelson, W.K.S. Chiu, Geometric sensitivity of electrochemical fin shape on three dimensional microstructure network conductivity analysis, *J. Power Sources* 291 (Sep. 2015) 181–194.
- [21] K.N. Grew, A.A. Peracchio, A.S. Joshi, J.R. Izzo, W.K.S. Chiu, Characterization and analysis methods for the examination of the heterogeneous solid oxide fuel cell electrode microstructure. Part 1: volumetric measurements of the heterogeneous structure, *J. Power Sources* 195 (24) (Dec. 2010) 7930–7942.
- [22] K.N. Grew, A.A. Peracchio, W.K.S. Chiu, Characterization and analysis methods for the examination of the heterogeneous solid oxide fuel cell electrode microstructure: Part 2. Quantitative measurement of the microstructure and contributions to transport losses, *J. Power Sources* 195 (24) (Dec. 2010) 7943–7958.
- [23] L. Holzer, B. Iwanschitz, Th Hocker, B. Münch, M. Prestat, D. Wiedenmann, U. Vogt, P. Holtappels, J. Sfeir, A. Mai, Th Graule, Microstructure degradation of cermet anodes for solid oxide fuel cells: quantification of nickel grain growth in dry and in humid atmospheres, *J. Power Sources* 196 (3) (Feb. 2011) 1279–1294.
- [24] B. Münch, L. Holzer, Contradicting geometrical concepts in pore size analysis attained with electron microscopy and mercury intrusion, *J. Am. Ceram. Soc.* 91 (12) (Oct. 2008) 4059–4067.
- [25] G.J. Nelson, A. Nakajo, B.N. Cassenti, M.B. DeGostin, K.R. Bagshaw, A.A. Peracchio, G. Xiao, S. Wang, F. Chen, W.K.S. Chiu, A rapid analytical assessment tool for three dimensional electrode microstructural networks with geometric sensitivity, *J. Power Sources* 246 (Jan. 2014) 322–334.
- [26] D. Chen, Z. Lin, H. Zhu, R.J. Kee, Percolation theory to predict effective properties of solid oxide fuel-cell composite electrodes, *J. Power Sources* 191 (2) (Jun. 2009) 240–252.
- [27] G.J. Nelson, K.N. Grew, J.R. Izzo Jr., J.J. Lombardo, W.M. Harris, A. Faes, A. Hessler-Wyser, J. Van herle, S. Wang, Y.S. Chu, A.V. Virkar, W.K.S. Chiu, “Three-dimensional microstructural changes in the Ni–YSZ solid oxide fuel cell anode during operation, *Acta Mater.* 60 (8) (May 2012) 3491–3500.
- [28] A. Faes, A. Hessler-Wyser, D. Presvytes, C.G. Vayenas, J. Van herle, “Nickel–Zirconia anode degradation and triple phase boundary quantification from microstructural analysis, *Fuel Cells* 9 (6) (Dec. 2009) 841–851.
- [29] D. Simwonis, F. Tietz, D. Stöver, Nickel coarsening in annealed Ni/8YSZ anode substrates for solid oxide fuel cells, *Solid State Ion.* 132 (3) (Jul. 2000) 241–251.
- [30] P. Tanasini, M. Cannarozzo, P. Costamagna, A. Faes, J. Van herle, A. Hessler-Wyser, C. Comminellis, Experimental and theoretical investigation of degradation mechanisms by particle coarsening in SOFC electrodes, *Fuel Cells* 9 (5) (Aug. 2009) 740–752.
- [31] D. Kennouche, Y.K. Chen-Wiegart, J.S. Cronin, J. Wang, S.A. Barnett, Three-dimensional microstructural evolution of Ni- yttria-stabilized zirconia solid oxide fuel cell anodes at elevated temperatures, *J. Electrochem. Soc.* 160 (11) (Jan. 2013) F1293–F1304.
- [32] Z. Jiao, N. Shikazono, Simulation of solid oxide fuel cell anode microstructure evolution using phase field method, *J. Electrochem. Soc.* 160 (6) (Jan. 2013) F709–F715.
- [33] X. Wang, A. Atkinson, Modeling microstructure evolution of Ni cermet using a cellular automaton approach, *J. Electrochem. Soc.* 161 (5) (Jan. 2014) F605–F614.
- [34] D. Bouvard, F.F. Lange, Relation between percolation and particle coordination in binary powder mixtures, *Acta Metall. Mater.* 39 (12) (Dec. 1991) 3083–3090.
- [35] P. Costamagna, P. Costa, V. Antonucci, Micro-modelling of solid oxide fuel cell electrodes, *Electrochim. Acta* 43 (3) (Jan. 1998) 375–394.
- [36] A. Bertei, C. Nicoletta, Percolation theory in SOFC composite electrodes: effects of porosity and particle size distribution on effective properties, *J. Power Sources* 196 (22) (Nov. 2011) 9429–9436.
- [37] R. Mendoza, I. Savin, K. Thornton, P.W. Voorhees, Topological complexity and the dynamics of coarsening, *Nat. Mater.* 3 (6) (Jun. 2004) 385–388.